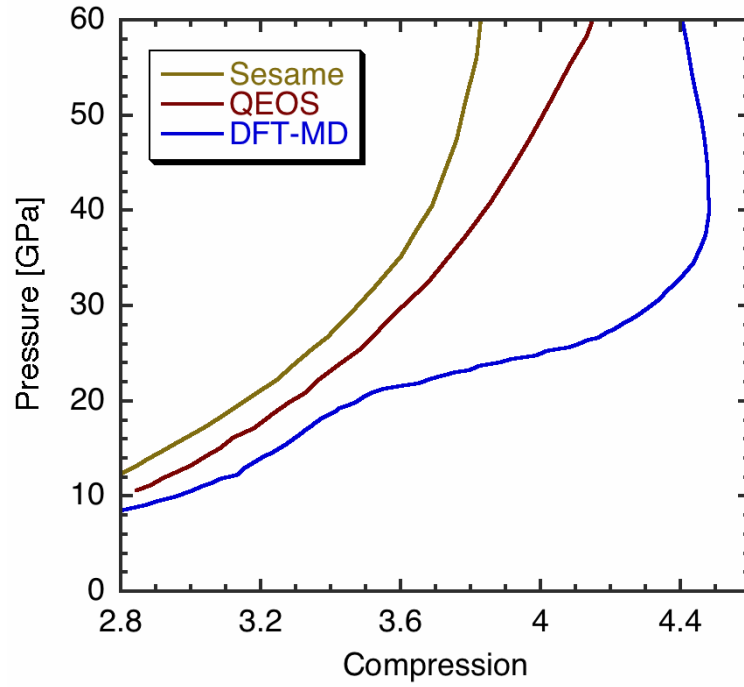**Supplementary Figure 1:** Si Li-α x-ray source function as measured with HOPG crystal spectrometer and image plates.

Supplementary Figure 2: The principal Hugoniot of Deuterium (ρ_0=0.17 g cm^{-3}) for Sesame, QEOS and the DFT-MD results of Holst et al. The Sesame and DFT-MD curves are used to establish limiting Hugoniot values in order to estimate uncertainty in compression resulting from uncertainty in equation of state.
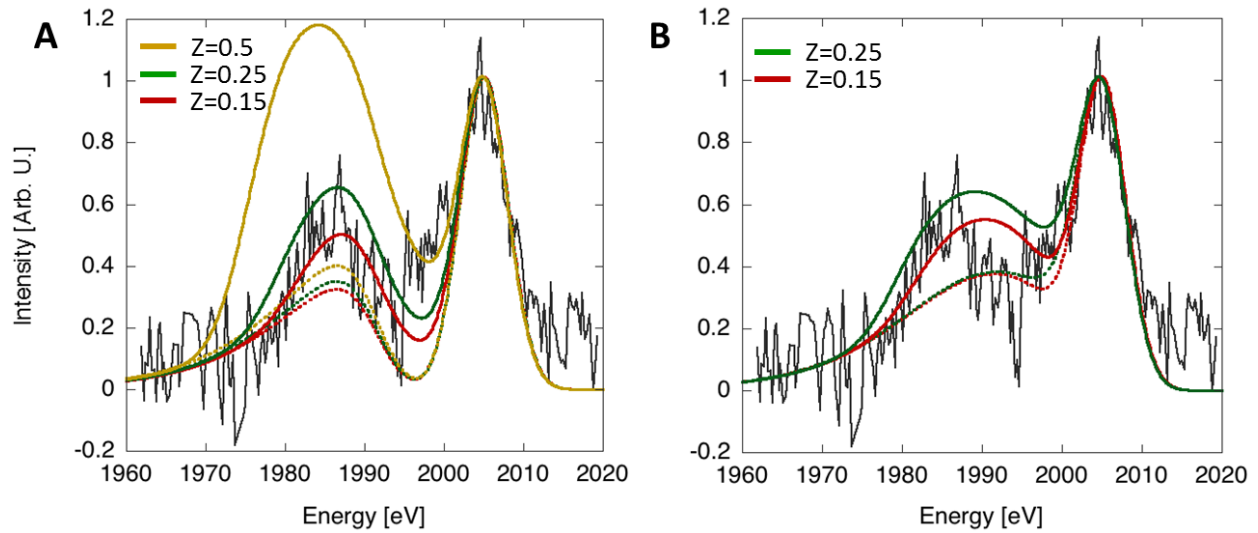
Supplementary Figure 3: Backscattering spectra and fits using two models for ionization potential depression (IPD). Solid curves represent the total scattering signal while dashed lines indicate contributions from bound-free and elastic scattering only. (A) Stewart-Pyatt IPD model for ionizations of $Z=0.15$ (red), 0.25 (green) and 0.5 (yellow). (B) Ecker-Kröll results for $Z=0.15$ (red) and 0.25 (green). 8 eV more continuum lowering effectively results in a shift of the bound-free scattering feature toward the elastic peak.
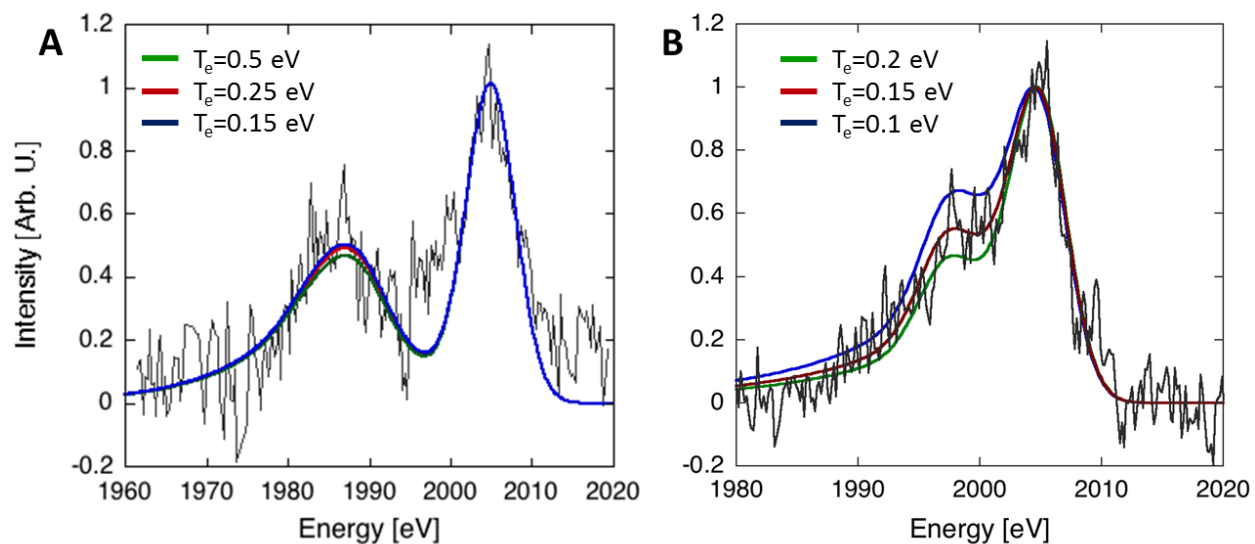
Supplementary Figure 4: Temperature dependence of x-ray scattering fits. (A) Backscattering data fit with three temperatures at $Z=0.15$. Very little change is seen for fits ranging from $T_e=0.15$-0.5 eV. (B) Plasmon scattering data fit at $Z=0.15$ with curves corresponding to $T_e=0.1$-0.2 eV. While the relative intensity of the plasmon feature drops with increasing temperature, the spectral position remains constant.
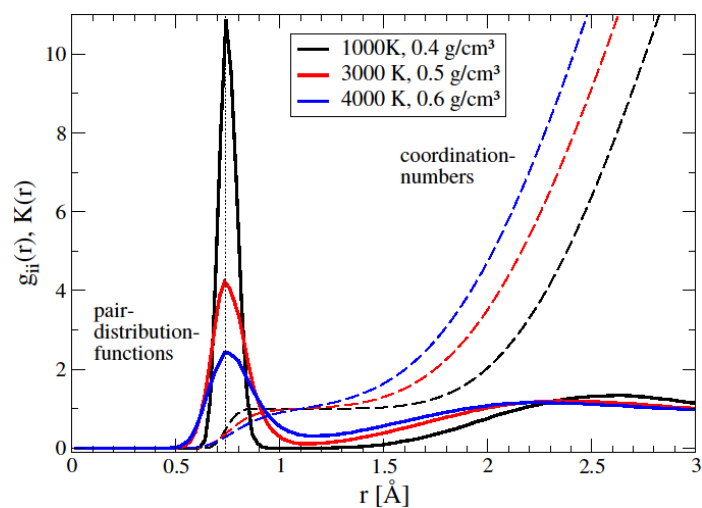
Supplementary Figure 5: Ionic pair distribution functions $g_{ii}(r)$ (solid) for several states along the Hugoniot curve together with their corresponding coordination number $K(r)$ (dashed). The dotted line indicates the molecular peak at 0.741 Å.
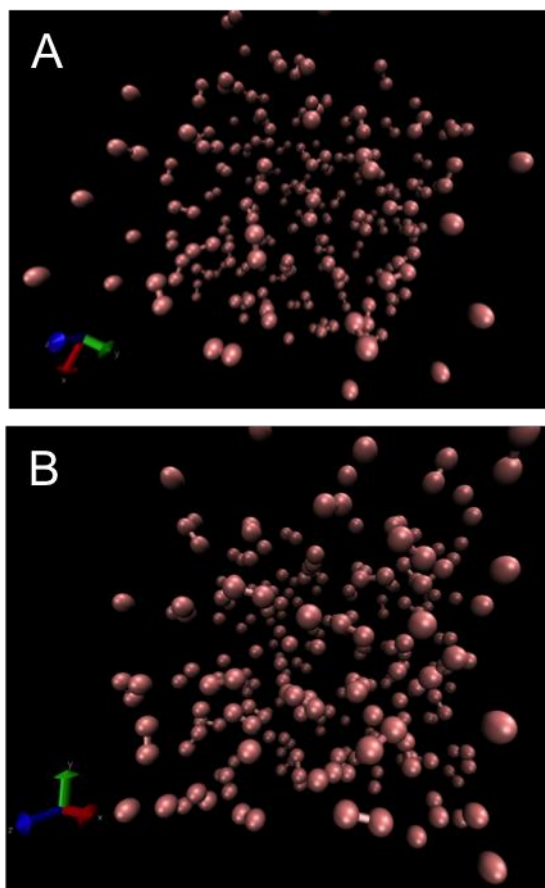
Supplementary Figure 6. (A) View inside the simulation box at 1000 K and 0.4 g cm^{-3} with α = 0.0066. **(B)** View inside the simulation box at 4000 K and 0.6 g cm^{-3} with α= 0.427.
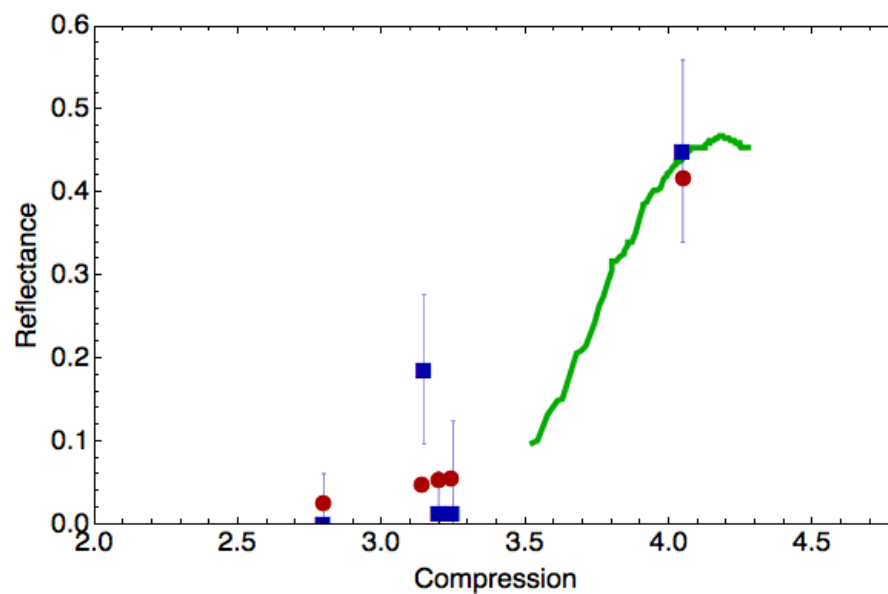
Supplementary Figure 7: Optical reflectivity in compressed D_2 previously measured by Celliers et al. (green) compared with reflectivity inferred from fits to x-ray scattering data (blue). Also shown is optical reflectivity inferred from DFT-MD simulations using the Kubo-Greenwood formalism (red).

Supplementary Note 1: Comparison with Reflectivity Measurements

The location of the transition to metal-like behavior has previously been inferred from measurements of optical reflectivity[1]. However, because the optical properties of dense hydrogen are quite complex during transition to the conducting state, it is difficult to infer ionization directly from reflectivity values and make a comparison to the measurements presented in the main text. In order to compare our results with these measurements, we instead used the Born-Mermin dielectric function corresponding to the best fit to the x-ray scattering spectrum and calculated the index of refraction of the plasma at the laser conditions used by Celliers et al. This allowed us to estimate the reflectivity corresponding to the measured x-ray spectrum. In addition, we have compared these results to reflectivities calculated within the Kubo-Greenwood formalism[2,3] by postprocessing the DFT-MD simulations at the points where XRTS measurements were made. The results are shown in Supplementary Figure 7, where the continuous line is an optical reflectivity measurement made in compressed D_2 using an 808 nm laser probe, the blue points represent reflectivities inferred from the x-ray scattering fits and the simulations are shown in red. The optical reflectivity and x-ray scattering results appear to be consistent when compared on this basis.

Supplementary Methods:

Experimental Configuration

The experiments were performed at the Janus Laser Facility, at Lawrence Livermore National Laboratory. The experimental configuration is illustrated in Figure 2 of the main text. A copper target held a reservoir of liquid deuterium near 19 K with initial deuterium density of $\rho_0=0.17\pm0.004$ g cm^{-3}. A single laser beam drove a shock into the deuterium with intensities of $\sim4\times10^{13}$ W cm^{-2} at the target in 2-6 ns long pulses. The beam used a phase plate to produce a round 600 μm diameter spot on target. The forward scattering measurements were made on deuterium shock-driven by a frequency-doubled 2 ns long laser pulse producing a wavelength of 527 nm at the target. The backscattering measurements were made operating the same laser at the 1054 nm fundamental, leading to higher intensities on target. These shots used pulses of up to 6 ns to sustain higher-pressure shocks in the target.

A second 527 nm beam was propagated at 90° to the drive beam, incident on a Si_3N_4 foil with an intensity of 1×10^{14} W cm^{-2}. This beam pumped the Si Ly-α line at 2005 eV, producing a bright x-ray source of bandwidth $\delta E/E=2\times10^{-3}$, sufficiently narrow to observe small plasmon shifts at fractional ionizations[4]. The probe pulse was delayed 10-20 ns after the rise of the drive beam, allowing the shock to traverse a distance of 350 μm to reach the center of the volume accessed by the x-ray diagnostic port. Conversion efficiency of laser energy into the Ly-α line was measured to be 0.2%, producing approximately 4×10^{12} x-ray photons at the target, sufficient for accurate single-shot measurements.

The x-rays were dispersed with Highly Ordered Pyrolytic Graphite (HOPG) crystal spectrometers, 24 x 70 mm curved with a radius of curvature (ROC) of 107 mm. The spectrometers operated in von Hamos geometry[5] collected and spectrally dispersed the scattered radiation onto Fuji BAS-TR025 image plates, resulting in a dispersion of 3.5 eV mm^{-1} and 4 eV instrument functions. The image plates were scanned at a resolution of 50 μm. The soft x-ray bremsstrahlung produced by the laser-target interaction was filtered by a 25 μm thick Be foil or a layer of aluminized plastic a few μm thick that was placed in front of the image plate. Of the $\sim4\times10^{12}$ photons produced, a fraction of 7×10^{-4} photons were scattered on a typical shot, consistent with the electron densities $\sim4\times10^{22}$ cm^{-3} measured at fractional ionizations. Supplementary Figure 1 shows the x-ray source function as measured with the HOPG and image

plates.

In dynamic x-ray scattering experiments, contributions from un-shocked material can contaminate the desired signal from the shocked sample. In our case, we note that the x-ray aperture is sufficiently small to localize the measurement to a volume mostly constrained to the shock front. This is further weighted by the higher scattering contribution from dense, hot material to confine the measurable signal to the shocked matter. We performed null tests on undriven targets to verify that there was no significant contribution from the target or unshocked volume. In addition, the plasmon data do not have the broadening or lower energy shifts we would expect from scattering from lower density hydrogen, and we are thus confident that our signal is collected from the compressed volume.

The mixing of pusher material into the field of view of the spectrometer would also be an important failure mode. However, we would expect this to be detectable as a spuriously large electron density and as a larger total photon signal at the detector. Neither signature was evident in our data.

Falk and coauthors have raised questions about combining VISAR measurements from a shock front with spatially integrated XRTS in similar experiments, particularly in the presence of gradients in plasma conditions[6]. While this is an important point, we note that the Falk experiment was designed to maximize scattering signal by scattering from a large volume of the target with an x-ray source antiparallel to the drive beam and thus including significant contributions from coronal plasma and all other plasma conditions present. We have attempted to control this with a narrower x-ray aperture. The Falk geometry also necessitated a design that did not use a solid density pusher on the target surface. As a result, Falk et al. report less uniform shock conditions than would otherwise be obtained, as well as measurable target preheat. We have avoided this outcome with an experimental design that allows for the use of an Al pusher. Significant variations in electron density would be expected to broaden the plasmon signal measurably and result in a less shifted spectral feature – something we do not detect in our data.

Deuterium Equation of State

The deuterium equation of state has generated a great deal of attention and controversy over the last two decades. In particular, the EOS along the primary Hugoniot has been studied extensively, with a focus on the region of maximum compressibility between about 30-200 GPa[7]. The early and widely used Sesame tables[8] predicted a relatively low compressibility (a "stiff" Hugoniot) while some laser experiments suggested a "softer" curve[9,10]. Updates to the Sesame model[11] and increasingly high resolution ab initio simulations[7] have led to more recent theoretical results between these two extremes.

Experiments at the Omega laser[12] and the Sandia Z-machine[13] have reported smaller differences in the measured Hugoniot. At pressures near 45 GPa, Hicks and coauthors find approximately a 12% difference in compression between the two experimental platforms, after correcting for differences in initial conditions and analysis. The error bars in these measurements are of a similar order, due to the inherent challenges of impedance matching in low density targets. The properties of quartz, typically used as an impedance matching standard in dynamic experiments, have also been shown to play an important role. Re-analysis with an improved quartz standard shifts the high-pressure Omega data toward lower compression and closer agreement with the Z results[14].

For data analysis and hydrodynamic calculations, we choose the quotidian equation of state (QEOS)[15] that yields compressions between the relatively stiff early Sesame curve[8] and a DFT-MD curve which is softer[16]. At low pressures ~15 GPa where most of our measurements are taken, the variation between these extremes is generally less than 10% – much of the current attention is focused on data above about 30 GPa and compressions greater than 4×. The three curves are plotted in Supplementary Figure 2 to show the relationship of the QEOS Hugoniot with these bounding curves. The difference between the QEOS Hugoniot and each of these curves is taken as an estimate of EOS-related uncertainty in the compression data plotted in Figure 6 of the main text, where this uncertainty has been added to the error in the VISAR and hydrodynamic calculations. We note that most of our data are taken at compressions of 3.2, where Supplementary Figure 2 suggests a range of pressure uncertainty from 13-19 GPa.

Analysis of x-ray scattering spectra

The recorded x-ray spectra were fit with a theoretical model that includes the spectral contributions of ions, free electrons and bound electrons. The model is based on the Chihara formula,

$$S(k,\omega) = |f(k) + q(k)|^2 S_{ii}(k,\omega) + Z_f S_{ee}(k,\omega) + Z_b \int d\omega' S_{ce}(k,\omega - \omega') S_S(k,\omega')$$

This formula describes the scattering spectrum as a combination of elastic scattering (first term), inelastic scattering from delocalized electrons (second term) and inelastic scattering from weakly bound electrons, including bound-free transitions to the continuum. Z_f and Z_b denote the number of delocalized (free) and weakly bound core electrons respectively.

The first term accounts for density correlations of electrons that follow the ion motion, including core electrons (represented by the ion form factor *f(k)*) and the screening electrons (*q(k)*). At the instrument resolutions obtained in our study, the ion-ion correlation function $S_{ii}(k,\omega)$ can be approximated $S_{ii}(k,\omega) = S_{ii}(k)\delta(\omega)$. The static ion structure factor is calculated in the Debye-Hückel approximation[17].

The second term describes the density correlations of free electrons. This term is often calculated in the random phase approximation (*RPA*), which assumes weak inter-particle interactions. Improvements have been introduced to account for strong coupling effects in dense matter in the form of the Born-Mermin approximation (*BMA*)[18]. This approach introduces a dynamic collision frequency *v(ω)* using an ansatz suggested by Mermin[19]. The collision frequency is calculated in the Born approximation[20]. Further improvements have been made by introducing local field corrections (*LFC*)[21]. Together, this *BMA-LFC* approach was shown to greatly improve the description of plasmon dispersion in warm, dense matter[22]. We use it in all of our analysis, although tests against *RPA* calculations show that the two models do not differ significantly at the density and temperature conditions explored in our study.

The third term describes bound-bound and bound-free scattering processes through the term $S_{ce}(k,\omega)$. There has been much recent work to improve the theoretical description of this term[23-25], which introduces significant model-dependence into the inelastic spectrum. In our case, we are primarily concerned with the treatment of ionization potential depression (IPD) which can

introduce plasma-parameter-dependent energy shifts and changes in shape to the bound-free component of the spectrum. In order to minimize the ambiguity of our fits, we compare calculations using two different models for IPD - the Stewart-Pyatt (SP)[26] and Ecker-Kröll (EK)[27] approaches. The results are plotted in Supplementary Figure 3.

In Supplementary Figure 3 (A), we show SP fits for ionizations of Z=0.15, 0.25 and 0.5 (solid lines) as well as dotted lines for those conditions representing only the bound-free and elastic scattering contributions. All fits were calculated for T_e=0.15 eV and ρ/ρ_0=3.2. Relative to the elastic scattering feature, the free-free scattering contribution grows much more rapidly with increasing ionization than the bound-free component. While IPD models affect the overall shape of the inelastic feature, this weak-scaling of the bound-free component with density means it has only a limited effect on the electron density inferred from the measurement. A best fit of Z=0.15 is found.

In Supplementary Figure 3 (B), we show EK fits for the same conditions and ionizations of Z=0.15 and 0.25. Dotted lines again correspond to bound-free and elastic scattering. In this case the peak of the bound-free feature is shifted toward E_0 relative to the SP case, a result we attribute to the much larger calculated lowering of the continuum in the case, ΔE_{EK}=10.2 eV compared with ΔE_{SP}=2.1 eV in the Stewart-Pyatt case. Nevertheless, we find Z=0.15 fits the spectrum best. The agreement in calculated density between these two cases gives us confidence that our inferred electron density is correct, notwithstanding the model-dependence of the bound-free feature.

We also tested the temperature dependence of the spectrum and found a very weak dependence in the intensity of the inelastic feature relative to the elastic. This is illustrated in Supplementary Figure 4 (A), where fits are shown for T_e=0.15, 0.25 and 0.5 eV at Z=0.15 and ρ/ρ_0=3.2. Because the scattering intensity is not a sensitive function of temperature, our stated T_e=0.15 eV measurement is only a rough estimate, albeit one that is consistent with forward scattering. Consequently, Compton scattering is only sensitive to Z; uncertainties in T_e do not affect the quoted values for Z.

Supplementary Figure 4 (B) shows the plasmon scattering data from Figure 4 of the main text with fits corresponding to Z=0.15 and temperatures of T_e=0.1, 0.15 and 0.2 eV. In this case, it is found that the intensity of the elastic feature changes with temperature relative to the plasmon

feature, but that the spectral location of the plasmon feature is temperature insensitive. This is to be expected at such low temperatures, where the thermal correction to the plasmon dispersion relation is too small to play a role. As a result, we are confident that the downshifted plasmon energy is a robust, first-principles measure of electron density.

The static structure factor of dense plasmas, particularly at small k-values in forward scattering experiments, remains an important and challenging research problem[28]. Our fits at T_e=0.15 eV are presented only as rough estimates that are model dependent, and are somewhat lower than the DFT-MD results of order ~0.3 eV at this point on the Hugoniot. However, the inferred ionization is insensitive to variations in temperature and consistent between the very different forward and backward scattering regimes.

Hydrodynamic Simulations

Radiation hydrodynamic simulations were performed using the package HYDRA[29]. The simulations are three-temperature (electron, ion and radiative) under the assumption of local thermodynamical equilibrium. The equation of state is similar to QEOS[15], with a Thomas-Fermi model for ionization and opacities. The laser absorption is modeled with ray tracing, the geometry is one-dimensional with a resolution of 0.25 μm. The equations for the multi-group radiation transport are solved in the diffusive limit, as is the thermal electron conduction, where a flux limiter of 0.05 is used.

We modeled the uncertainty in calculating the final compression by performing simulations for 20% deviations in laser intensity and taking bounding values from the relevant x-ray probe time. Although changes in laser drive conditions can cause significant deviations at early times, the shock decays to a similar set of plasma conditions at x-ray probe time. We note that the calculated shock velocities are consistent with the analytical scaling for laser driven one-dimensional shocks given in Ref. 30.

Simulation of Ionization and Dissociation

We outline the theoretical background of fluid variational theory (FVT) and the framework of density functional theory molecular dynamics (DFT-MD). Both methods were used to estimate

the dissociation degree $\alpha = N_D/(N_D + 2N_{D2})$, with the number of deuterium atoms N_D and deuterium molecules N_{D2} respectively, along the Hugoniot curve of deuterium, see[31]. The results for α are shown in Fig. 6 of the main text.

The FVT is a free energy minimization scheme for a mixture of hydrogen atoms and molecules, evaluating the chemical reaction $H_2 \Leftrightarrow H + H$ self-consistently (chemical models). The free energy F of the system is calculated on the basis of the Gibbs-Bogolyubov inequality $F \leq F_0 + \langle \Phi - \Phi_0 \rangle_0$ that states that F is less or equal the sum of the free energies of a reference system F_0 (here a hard sphere system) and the mean value of the difference of two interaction potentials evaluated over the reference states. In our case the reference hard sphere potential Φ_0 and effective two-particle potentials, namely the exponential-6 potentials Φ (see Ref. 32 for the molecules and Ref. 33 for the atoms) for the real system are used, see Ref. 34.

The equation of state (EOS) and α are direct outputs of the FVT calculation. Since the underlying Hugoniot curve is based on DFT-MD calculations for deuterium, the FVT data have to be mapped to it. Therefore we scaled the density of our FVT hydrogen EOS by a factor of 2, to adjust it to deuterium. We then extracted the FVT EOS points with the respective (FVT)-α according to the EOS points of the underlying DFT-MD Hugoniot curve.

In contrast to FVT, the DFT-MD framework is based on a strictly physical picture. Bound states or other long-living correlations between the electrons and ions are not regarded as new species as in the chemical picture. According to the Born-Oppenheimer approximation the treatment of the ions is classical in the MD and the properties of the electron system are evaluated on the quantum level using the DFT at finite temperatures[35].

For our simulations we use the VASP program package[36-38]. To calculate the Coulomb interactions between the electrons and ions more efficiently, projector-augmented wave potentials[39,40] are used with a converged energy cutoff of 1200 eV.

The forces that act on the ions are derived via the Hellmann-Feynman theorem at each MD step. This procedure is repeatedly performed in a cubic simulation box with periodic boundary conditions for several thousand MD steps of 0.2 fs to 1 fs duration so that the total simulation time amounts up to 8 ps. The ion temperature is controlled with a Nosé thermostat[41]. The most crucial approximation within the DFT is the choice of the exchange-correlation functional for

which we use the one of Perdew, Burke, and Ernzerhof (PBE)[42], a parametrization of the generalized gradient approximation (GGA).

We ensure convergence of our simulation runs with respect to the energy cutoff for the plane wave basis set, the particle number and the **k**-point sets applied for the evaluation of the Brillouin zone. In detail we used 256 atoms and the Baldereschi mean value point[43].

The dissociation degree for each EOS point along the Hugoniot curve is estimated via the coordination number $K(r)$, a weighted integral over the pair correlation function $g_{ii}(r)$ of the ions, see Ref. 13:

$$K(r) = \frac{N-1}{V} \int_0^r 4\pi r'^2 \, g_{ii}(r')dr'$$

N is the numer of simulated ions and V the volume of the simulation box. Twice the value of $K(r)$ at the molecule peak, indicated by the dotted line at 0.741Å in Supplementary Figure 5, is equal to the number of ions bound to a molecule: $2K(r)=2N_{D2}/(2N_{D2}+N_D)$. Hence the relation between the coordination number and the dissociation degree is $\alpha = 1 - 2K(r)$. Also shown in Supplementary Figure 5 are $g_{ii}(r)$ and $K(r)$ for three EOS points along the Hugoniot curve.

The simulation box at 1000 K and 0.4 g cm^{-3} is shown in Supplementary Figure 6 (A) with α= 0.0066. As is shown, all ions in the box are bound in molecules. The single ions at the edge are due to the finite box. The respective molecule partner is found in the next box. A box visualizing a much higher dissociation degree of α=0.427 at 4000 K and 0.6 g cm^{-3} is shown in Supplementary Figure 6 (B). Just about half of the ions are bound to molecules here, leading to a lower molecule peak and a lower coordination number, see Supplementary Figure 5.

Supplementary References:

1. Celliers, P. M. *et al*. Shock-induced transformation of liquid deuterium into a metallic fluid. *Phys. Rev. Lett.* **84**, 5564–5567 (2000).

2. Kubo, R. Statistical-Mechanical Theory of Irreversible Processes. I. General Theory and Simple Applications to Magnetic and Conduction Problems *J. Phys. Soc. Jpn.* **12**, 570 (1957).

3. Greenwood, D. A. The Boltzmann Equation in the Theory of Electrical Conduction in Metals *Proc. Phys. Soc. London* **71**, 585-596 (1958).

4. Davis, P., Döppner, T., Glenzer, S. H., Falcone, R. W. & Unites, W. An apparatus for the characterization of warm, dense deuterium. *JINST* **7**, 02004 (2012).

5. Urry, M. K., Gregori, G., Landen, O.L., Pak, A. & Glenzer, S. H. X-ray probe development for collective scattering measurements in dense plasmas. *J. Quant. Spectr. Rad. Trans.* **99**, 636-648 (2006).

6. Falk, K. *et al*. Comparison between x-ray scattering and velocity-interferometry measurements from shocked liquid deuterium. *Phys. Rev. E* **87**, 043112 (2013).

7. McMahon J. M., Morales M. A., Pierleoni C. & Ceperley D. M. The properties of hydrogen and helium under extreme conditions. *Rev. Mod. Phys.* **84**, 1607–1653 (2012).

8. Kerley, G. I. Equation of state and phase diagram for dense hydrogen. *Phys. Earth Planet. Inter.* **6**, 78-82 (1972).

9.Collins, G. W. *et al*. Measurements of the Equation of State of Deuterium at the Fluid Insulator-Metal Transition. *Science* **281**, 1178-1181 (1998).

10. M. Ross, Linear mixing model for shock-compressed liquid deuterium. *Phys. Rev. B* **58**, 669-677 (1998).

11. Kerley, G. I. Sandia National Laboratories Technical Report No. SAND2003-3613 (2003).

12. Hicks, D. G. *et al*. Laser-driven single shock compression of fluid deuterium from 45 to 220 GPa. *Phys. Rev. B* **79**, 014112 (2009).

13. Knudson, M. D. *et al.* Principal Hugoniot, reverberating wave, and mechanical reshock measurements of liquid deuterium to 400 GPa using plate impact techniques. *Phys. Rev. B* **69**, 144209 (2004).

14. Knudson, M. D. & Desjarlais, M. P. Shock Compression of Quartz to 1.6 TPa: Redefining a Pressure Standard. *Phys. Rev. Lett.* **103**, 225501 (2009).

15. More, R. M., Warren, K. H., Young, D. A. & Zimmerman, G. B. A new quotidian equation of state (QEOS) for hot dense matter. *Phys. Fluids* **31**, 3059-3078 (1988).

16. Holst, B., Redmer, R. & Desjarlais, M. P. Thermophysical properties of warm, dense hydrogen using quantum molecular dynamics simulations. *Phys. Rev. B* **77**, 184201 (2008).

17. Ichimaru, S. *Basic Principles of Plasma Physics: A Statistical Approach* (W.A. Benjamin, Reading, MA, 1973).

18. Redmer, R., Reinholz, H., Röpke, G., Thiele, R. & Höll, A. Theory of X-Ray Thomson Scattering in Dense Plasmas. *IEEE Trans Plasma Sci.* **33**, 77-84 (2005).

19. Mermin, N. D. Lindhard dielectric function in the relaxation-time approximation. *Phys. Rev. B* **1**, 2362–2363 (1970)

20. Thiele, R. *et al.* Plasmon resonance in warm dense matter. *Phys. Rev. E* **78**, 026411 (2008).

21. Fortmann C., Wierling A. & Röpke G. Influence of local-field corrections on Thomson scattering in collision dominated two-component plasmas. *Phys. Rev. E* **81**, 026405 (2010).

22. Neumayer, P. *et al.* Plasmons in Strongly Coupled Shock-Compressed Matter. *Phys. Rev. Lett*. **105**, 075003 (2010).

23. Johnson W. R., Nilsen J. & Cheng K. T. Resonant bound-free contributions to Thomson scattering of X-rays by warm dense matter. *High Energy Density Phys.* **9**, 407-409 (2013).

24. Souza A. N., Perkins D. J., Starrett C. E., Saumon D. & Hansen S. B. Predictions of x-ray scattering spectra for warm dense matter. *Phys. Rev. E* **89**, 023108 (2014**).

25. Fletcher, L. B. *et al*. Observations of Continuum Depression in Warm Dense Matter with X-Ray Thomson Scattering. *Phys. Rev. Lett*. **112**, 145004 (2014).

26. Stewart, J. C. & Pyatt Jr., K. D. Lowering of Ionization Potentials in Plasmas *Astrophys. J*. **144**, 1203-1211 (1966).

27. Ecker, G. & Kröll, W. Lowering of the Ionization Energy for a Plasma in Thermodynamic Equilibrium. *Phys. Fluids* **6**, 62-69 (1963).

28. Gericke, D. O., Vorberger, J., Wünsch, K. & Gregori, G. Screening of ionic cores in partially ionized plasmas within linear response. *Phys. Rev. E* **81**, 065401 (2010)

29. Marinak, M. M. *et al*. Three-dimensional simulations of Nova high growth factor capsule implosion experiments. *Phys. Plasmas* **3**, 2070-2076 (1996).

30. Drake, P. *High-Energy-Density Physics: Fundamentals, Inertial Fusion, and Experimental Astrophysics* (Springer, Berlin, 2006).

31. Holst, B., Redmer, R., Gryaznov, V., Fortov, V. & Iosilevskiy, I. Hydrogen and deuterium in shock wave experiments, ab initio simulations and chemical picture modeling. *Eur. Phys. J. D* **66**, 104 (2012).

32. Ross, M., Ree, F. H. & Young, D. A. The equation of state of molecular hydrogen at very high density. *J. Chem. Phys.* **79**, 1487-1494 (1983).

33. Ree, F. H. in *Shock Waves in Condensed Matter - 1987*, edited by S. Schmidt and N. Holmes (Elesevier, New York, 1988) pp. 125–130.

34. Juranek, H., Redmer, R. & Rosenfeld, Y. Fluid variational theory for pressure dissociation in dense hydrogen: Multicomponent reference system and nonadditivity effects. *J. Chem. Phys*. **117**, 1768-1774 (2002).

35. Mermin, N. D. Thermal Properties of the Inhomogeneous Electron Gas. *Phys. Rev.* **137**, 1441-1443 (1965).

36. Kresse, G. & Hafner, J. *Ab initio* molecular dynamics for liquid metals. *Phys. Rev. B* **47**, 558-561 (1993).

37. Kresse, G. & Hafner, J. *Ab initio* molecular-dynamics simulation of the liquid-metal–amorphous-semiconductor transition in germanium. *Phys. Rev. B* **49**, 14251-14269 (1994).

38. Kresse, G. & Furthmüller, J. Efficient iterative schemes for *ab initio* total-energy calculations using a plane-wave basis set. *Phys. Rev. B* **54**, 11169-11186 (1996).

39. Blöchl, P. E. Projector augmented-wave method. *Phys. Rev. B* **50**, 17953-17979 (1994).

40. Kresse, G. & Joubert, D. From ultrasoft pseudopotentials to the projector augmented-wave method. *Phys. Rev. B* **59**, 1758-1775 (1999).

41. Nosé, S. A unified formulation of the constant temperature molecular dynamics methods. *J. Chem. Phys*. **81**, 511-519 (1984).

42. Perdew, J. P., Burke, K. & Ernzerhof, M. Generalized gradient approximation made simple. *Phys. Rev. Lett*. **77**, 3865-3868 (1996).

43. Baldereschi, A. Mean-value point in the Brillouin zone. *Phys. Rev. B* **7**, 5212-5215 (1973).